The Effects That Cardiac Motion has on Coronary Hemodynamics and Catheter Trackability Forces for the Treatment of Coronary Artery Disease: An *In Vitro* Assessment

Liam Morris, Paul Fahy, Florian Stefanov, and Ronan Finn

Galway Medical Technologies Centre, Department of Mechanical and Industrial Engineering, Galway Mayo Institute of Technology, Galway, Ireland

Associate Editor Ajit P. Yoganathan oversaw the review of this article.

Abstract—The coronary arterial tree experiences large displacements due to the contraction and expansion of the cardiac muscle and may influence coronary haemodynamics and stent placement. The accurate measurement of catheter trackability forces within physiological relevant test systems is required for optimum catheter design. The effects of cardiac motion on coronary flowrates, pressure drops, and stent delivery has not been previously experimentally assessed. A cardiac simulator was designed and manufactured which replicates physiological coronary flowrates and cardiac motion within a patient-specific geometry. A motorized delivery system delivered a commercially available coronary stent system and monitored the trackability forces along three phantom patient-specific thin walled compliant coronary vessels supported by a dynamic cardiac phantom model. Pressure drop variation is more sensitive to cardiac motion than outlet flowrates. Maximum pressure drops varied from 7 to 49 mmHg for a stenosis % area reduction of 56 to 90%. There was a strong positive linear correlation of cumulative trackability force with the cumulative curvature. The maximum trackability forces and curvature ranged from 0.24 to 0.87 N and 0.06 to 0.22 mm^{-1} respectively for all three vessels. There were maximum and average percentage differences in trackability forces of (23–49%) and (1.9–5.2%) respectively when comparing a static pressure case with the inclusion of pulsatile flow and cardiac motion. Cardiac motion with pulsatile flow significantly altered (p value <0.001) the trackability forces along the delivery pathways with high local percentage variations and pressure drop measurements.

Keywords—Coronary artery disease, Endovascular stents, Trackability, Pressure drop, Curvature, Cardiac motion.

Address correspondence to Liam Morris, Galway Medical Technologies Centre, Department of Mechanical and Industrial Engineering, Galway Mayo Institute of Technology, Galway, Ireland. Electronic mail: liam.morris@gmit.ie

INTRODUCTION

The coronary arterial tree experiences large displacements due to the contraction and expansion of the cardiac muscle. Simplifications of the modeling process are desirable due to the cost involved in replicating cardiac muscle motion with coronary flow rates for *in vitro* studies and the increased computational expense for numerical simulations. Previous investigators have numerically analyzed the effects of modeling simplifications on various hemodynamic parameters within the aortic arch,[24] abdominal aortic aneurysms,[9,19,29,37,38] carotids,[30,52] and coronaries.[16,31,32,45,51] Ene *et al.*[9] highlighted the need for applying fluid structure interaction methods when assessing flow and wall shear stress patterns while static finite element analysis was sufficient for assessing von misses stress within the arterial wall. Also, it was shown numerically that coronary wall motion and the phasic relation between the flow rates and arterial wall dynamics significantly influence the temporal variations in wall shear stress and flow patterns,[31,32,45,51] while the time-averaged wall shear stress (WSS) was not appreciably affected.[51] To date, no *in vitro* flow assessment exists which assesses the hemodynamic effects along coronary vessels due to cardiac motion.

The delivery of coronary endovascular stents to the vicinity of a lesion is paramount for the successful treatment of coronary artery disease. The ease with which a catheter follows a guidewire through a blood vessel is termed "trackability".[54] Trackability describes the deliverability of a stent system along a curved vessel up to the lesion[36] which characterizes the frictional forces that are felt by the clinician during catheter placement.[11] The accurate measurement of

catheter trackability forces within physiological relevant test systems is required for optimum catheter design. Most medical device companies assess the trackability forces for further catheter delivery development.[2] Excessive catheter delivery forces can produce vasoconstriction and injury, resulting in reactive intimal proliferation or distal embolisation associated with end-organ ischemia and infarction.[4,5]

To date, *in vitro* coronary trackability studies have been examined along two-dimensional rigid pathways comprising of various bends within plexiglass,[34] high density polyethylene,[36] acrylic,[15] soft vinyl chloride[42] tubing and three-dimensional rigid pathways within polytetrafluoroethylene tubing,[54] and polyethylene.[11] These trackability studies did not take into account the physiological conditions of pulsatile flow, arterial wall
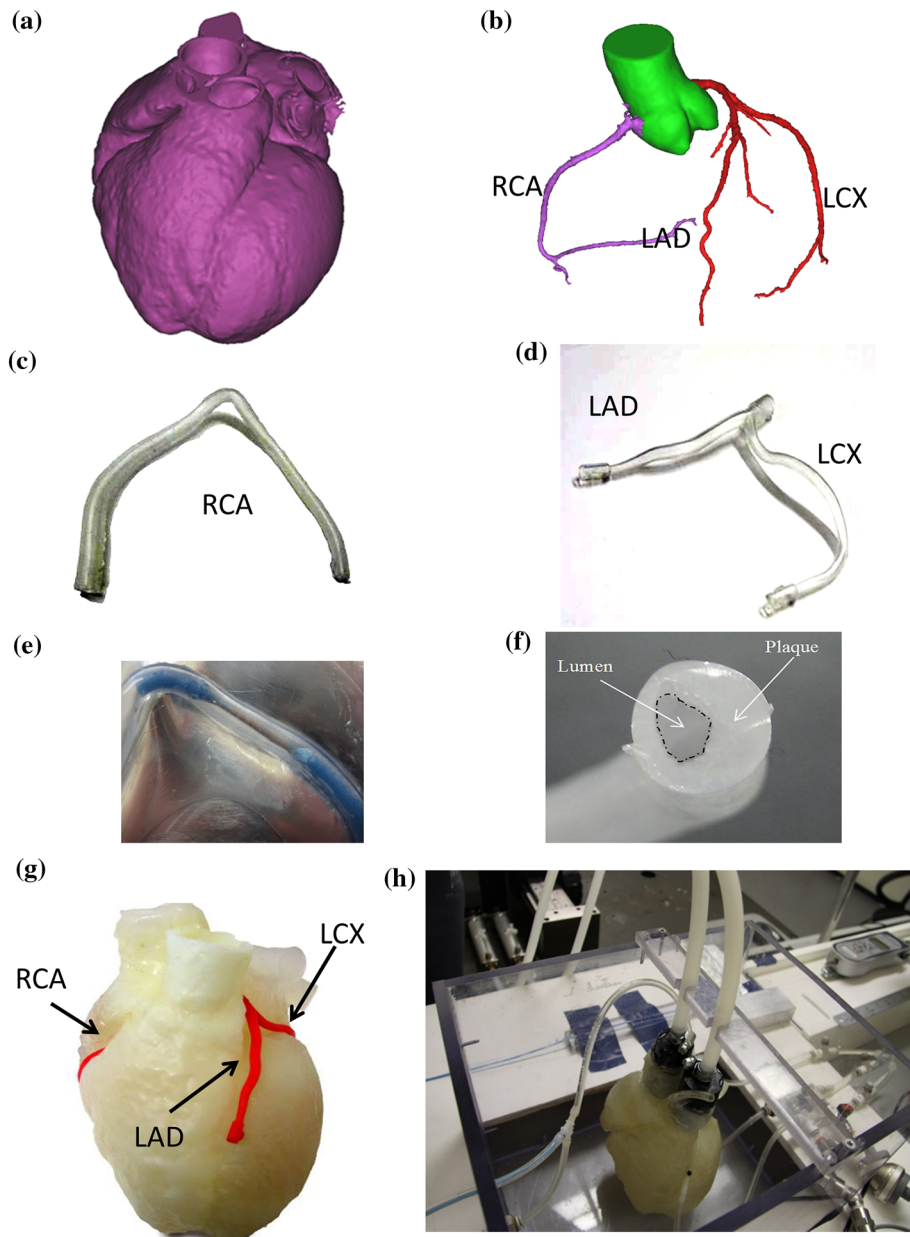

FIGURE 1. (a) 3D triangulated fitted surface of the cardiac muscle, (b) 3D triangulated fitted surface of the left and right coronary arteries, (c) thin-walled flexible polyvinyl alcohol cryogel right coronary artery, (d) thin-walled flexible polyvinyl alcohol cryogel left coronary artery, (e) steel wire positioned within coronary phantom, (f) replicated calcified stenosis within RCA, (g) hollow flexible cardiac model with coronary vessels attached within the atrio and interventricular grooves, (h) cardiac model housed within a polycarbonate box.

compliance and cardiac wall motion as would be experienced within patient-specific cases. Other investigators have assessed various arterial geometrical parameters within large[26,27,46,49] to small sized[6,22,23,26,28,47] vessels, in an attempt to facilitate endovascular interventional planning. None of these studies have assessed the possible impact that physiological conditions may have on the positioning of coronary stents.

The objective of this study was to design and manufacture a cardiac flow simulator based on medical images capable of assessing the significance that cardiac wall motion and coronary flow rates have on coronary hemodynamics and trackability forces. Three flowrate waveforms were replicated for the left/right coronary vessels with the inclusion of a superimposed cardiac motion and assessing the effects on outlet flowrates and pressure drops. An evaluation of the effects of varying degrees of stenosis has on pressure drops under steady and pulsatile flow conditions were assessed. Also, a motorized delivery system monitored the trackability forces and delivered a commercially available coronary stent system along three phantom patient-specific thin walled compliant coronary vessels under no flow, pulsatile flow and dynamic cardiac wall conditions. To date, no such study exists which examines trackability forces, within the coronary vessels, under pulsatile flow and dynamic cardiac wall motion.

MATERIALS AND METHODS

Patient-Specific Cardiac Geometry Reconstruction

A cardio-gated multi-detector computed tomography scanned data set of a cardiac muscle, with no pathological defects comprising of the right (RCA) and left (LCA) coronary arteries, was obtained from the imaging software company, Materialise (Belgium) for a 57 year old male. This data set had a pixel size of 0.488 mm with a slice increment of 0.625 mm. The LCA bifurcated into the left anterior descending artery (LAD) and the left circumflex artery (LCX). A three-dimensional triangulated fitted surface of the cardiac muscle with the four chambers and the myocardium (Fig. 1a), and the left/right coronary arteries (Fig. 1b) were obtained by thresholding and segmentation techniques within the commercial available imaging software package Mimics V13.1 (Materialise, Leuven, Belgium). The cartesian co-ordinate of the centrelines and corresponding orthogonal best-fit diameters for both the RCA and LCA were generated at 1 mm increments. These centrelines and diameters were further smoothed by least square polynomial fits within Matlab v7.1.0. (Mathworks, USA). The degree of polynomial for each operation was based on the variance of the data sets as previously explained.[24] These coronary vessels had lumen diameter variations of 2–5 mm, with centreline lengths of the RCA, LAD, and LCX being 140, 67 and 100 mm respectively. The centreline curvature $k(l)$ was parameterised in terms of the vessel's centreline length (l) and was calculated at 1 mm increments using a standard formula from the Frenet–Serret theory of differential geometry given by

$$k(l) = \frac{|r'(l) \times r''(l)|}{[r'(l)]^3}, \qquad (1)$$

where $r'(l)$ and $r''(l)$ are the first and the second derivatives of the vessels centreline with respect to the centreline length (l) and $|r'(l) \times r''(l)|$ is the absolute value of the cross product. Table 1 summarizes these geometrical parameters.

Coronary Arteries Phantom Fabrication

The lost wax technique was used to create the flexible coronary models. This consisted of generating molds on a CAD/CAM software Pro-Engineer/Manufacture (PCT, Wildfire 4.0, PTC, Needham, MA) and machining two sets of aluminum molds on a 4-axis CNC milling centre (Hurco UK, VM1). The first set of molds created the inner low melting point alloy (LMPA) core. The LMPA cores were inserted into a second set of outer molds. The outer arterial wall was replicated by a hydrogel polymer mixture comprising of dimethyl sulfoxide (Sigma-Aldrich, Ireland Ltd, Ireland) and de-ionized water in a ratio of 4:1 by weight, to which 15% of polyvinyl alcohol powder by

TABLE 1. Summary of curvature, diameter, and length for the RCA, LAD, and LCX vessels.

Parameter	Vessel					
	RCA		LAD		LCX	
	Range	Mean ± SD	Range	Mean ± SD	Range	Mean ± SD
Curvature (mm^{-1})	0.0025–0.2229	0.0387 ± 0.0427	0.0012–0.1791	0.0402 ± 0.0287	0.0017–0.0767	0.0303 ± 0.0169
Diameter (mm)	2.476–3.987	3.268 ± 0.573	1.492–4.939	2.615 ± 0.810	2.266–3.815	2.903 ± 0.308
Length (mm)	140		67		100	

weight was added. Once injected into the mold, the hydrogel was subjected to six freeze–thaw cycles of −17 °C to 4 °C for a minimum of 12 h per cycle. Once cured the mixture became a polyvinyl alcohol cryogel (PVA-C) with a Young's Modulus range of 210–370 kPa as tested on a uni-axial tensile testing machine (Instron 5544, UK) equipped with ±10 N static load cell and a standard video extensometer. The LMPA was removed resulting in flexible thin-walled coronary vessels (Figs. 1c and 1d). A constant compliance value along each arterial length was manufactured by varying the wall thickness from 1.00 to 0.47 mm for all three models. The compliance values were measured at different locations ($n = 7$) along each model by subjecting the models to pulsatile flow conditions and simultaneously measuring the pressure with a 3F pressure catheter (Scisence Inc., Canada) and outer wall diameters with a CCD camera (Dalsa 4M30, Dalsa USA, Falcon 4M30) and analyzed within the Vision Assist Software (National Instruments, UK). The models had a compliance value range of 0.021–0.037 mm^2/mmHg at physiological pressures of 80–120 mmHg which was within the physiological compliance range of 0.01–0.06 mm^2/mmHg as acquired clinically by endovascular ultrasound.[1,39,48] Each model was dissected at 5 mm increments along its length, providing 12–20 cross sectional slices for each vessel segment. Each cross-section was placed under a calibrated 4 Megapixel CCD camera (Dalsa USA, Falcon 4M30) with a resolution of 0.0211 mm per pixel and analyzed with the Vision Assistant software (National Instruments, UK). 12 values were obtained radially and these were averaged for each section. The average circumferential wall thickness variation was 7%. The co-efficient of friction was 0.04–0.06 as tested by an in-house co-efficient of friction testing fixture which was attached to the tensile testing machine as specified within the BS ISO 8295; 2004 standard for determining the co-efficient of friction for plastics, film and sheeting. This co-efficient of friction values for PVA-C was within the range of 0.01–0.05 found by[21,33] and within the arterial values of 0.03–0.06.[8,43] Three sized diameter stenosis of 2, 1.5, and 1 mm corresponding to % area reductions of 56, 75, and 89% respectively were created within the RCA coronary model (Figs. 1e and 1f). The calcified plaque was replicated with a silicone elastomer Elastosil M4641 (Wacker, Germany) which had a stiffness value of 1800 ± 200 kPa that was within the range for calcified plaques of 2190 ± 990 kPa.[18] Steel wires were machined to the required diameters with a length of 15 mm and positioned within the RCA vessel (Fig. 1e). This length was within the *in vivo* length values of 16 ± 8.19 mm reported by Kousera *et al.*[17] The silicone elastomer was injected through the wall thus filling the void. Once cured the wire was removed leaving the stenosis (Fig. 1f).

Cardiac Muscle Phantom Replication

A two part silicone mixture (Essil 291/292, Axson, France) with the addition of 55% silicone fluid (Notcutt 200/5CS, UK) by weight was used to replicate the heart muscle. The Young's modulus was 116 kPa. This Young's modulus was within the cardiac muscular tissue range as found by Yin *et al.*[50] for uni-axial tensile testing data for human myocardium in the fibrous direction. A rigid solid polycarbonate outer cardiac wall was produced using stereolithography (SLA) with a slice thickness of 0.05 mm and the inner right and left ventricular lumens were manufactured using by fused deposition modeling (FDM) (Stratasys, Prodigy Plus FDM, Stratasys Inc USA) from ABS plastic with a slice thickness of 0.17 mm. The rapid prototyped (RP) cardiac models were reversed cast to produce wax and silicone replicas. The parts were positioned within a casting box which was filled with molding silicone (Essil 291/292 with 30% added silicone fluid) to produce three silicone blocks. This silicone mixture was degassed in a vacuum chamber for 30 min and cured for 24 h at room temperature. These blocks were then split by a scalpel and the RP parts removed, producing three sets of silicone molds. The ventricle molds incorporated fillers for recreating wax castings while the cardiac mold contained injection ports and risers for injection molding. The ventricles were produced by pouring molten wax (Hyfill B659, Remet, UK) at 80 °C into a filler hole located in the top of the mold. Once cured, the silicone mold was opened and the wax replicas removed. Both the right and left wax ventricular replicas were positioned within the outer silicone mold using the T-shaped locators. Silicone (Essil 291/292) with 55% added silicone fluid was mixed, degassed and injected into the silicone mold using a handheld syringe pump. Once cured, the wax cores were melted at a temperature of 80 °C to produce the hollow heart model as shown in Fig. 1g. The wall thickness of the left ventricle varied from 7 to 12 mm, and the right ventricle varied from 3 to 5 mm. This variation in wall thicknesses was generated directly from the CT scanned data sets. The PVA-C coronary models were positioned within the atrio and interventricular grooves between the ventricles and atriums upon the silicone cardiac model and adhered within the groves by silicone (Essil 291/292 with 55% silicone fluid). The cardiac model was housed within a polycarbonate box for trackablitiy testing (Fig. 1h).

Physiological Flow Simulation

The coronary flowrate waveforms with a period of 0.85 s were simulated by a programmable ball screw linear stage (ATS 15010-2, Aerotech Inc, UK) comprising of a built in 1000 line noncontact rotary encoder, capable of velocities up to 115 mm/s, with an accuracy of $+2, -5$ μm carrying a maximum load of 45 kg. A double acting piston pump configuration was connected onto the linear stage to accurately replicate the complex coronary waveforms. The coronary blood pressure was controlled by a throttle valve downstream of the model section and monitored by in-line pressure transducers (KH-68075-40, Cole-Parmer, USA). The pressure transducers were positioned 10 mm upstream and downstream of each vessel's inlet and outlet respectively connected to luer lock fittings. The coronary flow rates were validated by an ultrasonic clip-on flow sensor (ME-5PXL, Transonic Systems Inc, USA) in which the calibrated tygon tubing for the clip-on flow sensors were positioned just before and after the the upstream and downstream luer lock pressure connections respectively. Pneumatic in-line flow connections and tubes provided a smooth and leakfree interface within the flow system. The blood was mimicked with a water/glycerol mixture that had a viscosity of 0.004 Pa s as found by a digital viscometer (Brookfield DV-II +PRO, Brookfield laboratories, Middleboro, MA, USA).

Cardiac Motion Simulation

The two ventricles were connected to a closed pumping system which simulated the ventricular motion. Each ventricle was connected to a piston pump (SMC Pneumatics, Ireland Ltd) using a non-compliant tubing filled with a fixed volume of deionised water. The pump's displacement was controlled by a second linear actuator (Aerotech Inc, UK), which controlled ventricular contraction (systole) and expansion (diastole). This closed system displaced the required stroke volume. A phase lag of one-fifth of a cardiac cycle[12] between the coronary flow rates and ventricular displacement was imposed. A data acquisition card (USB-6009, National Instruments, Berkshire, UK) acquired the input data from the flow and pressure sensors with a sampling rate of 500 Hz. A dedicated software program was written in Labview V8.6 (National Instruments, Berkshire, UK) controlled, monitored and displayed all the measured parameters. The full configuration of the coronary and cardiac circuit with data acquisition/control are shown in Figs. 2a and 2b.

Catheter Delivery

The catheter trackability forces were assessed within each vessel using a commercially available balloon expandable coronary stent system. The stent was delivered through a 7F (Ø2.33 mm) guide catheter over a Ø0.36 mm floppy tip guidewire. The proximal
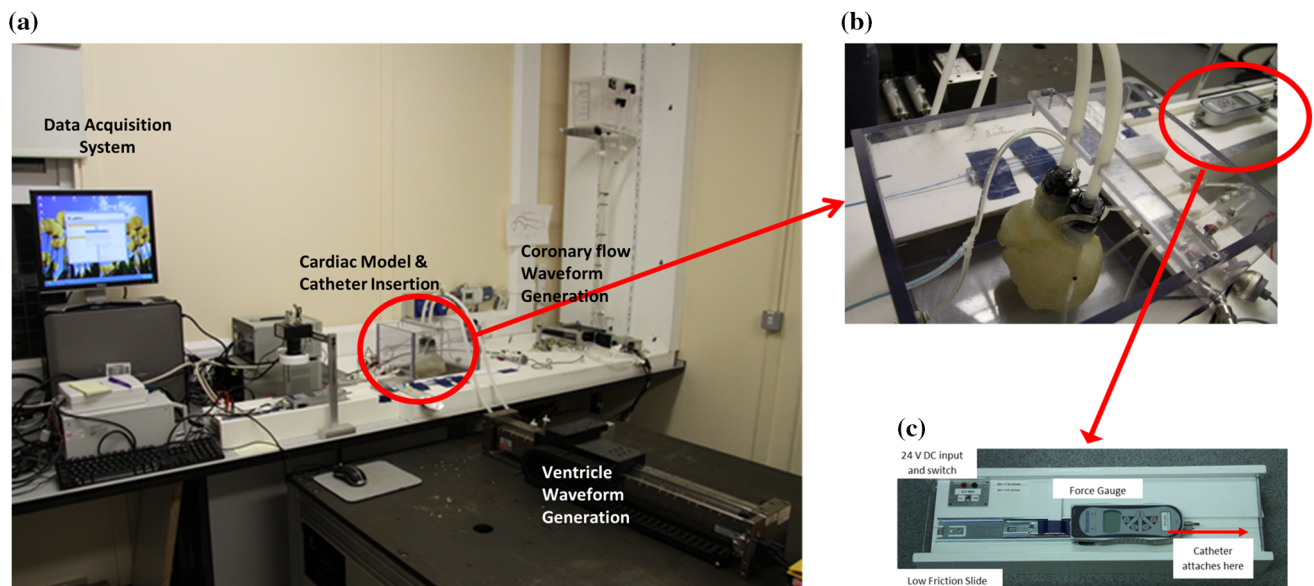

FIGURE 2. (a) cardiac simulator set-up, (b) zoomed in view of the attached cardiac phantom muscle within the simulator, and (c) motorized catheter delivery rig.

end of the catheter was attached to a motorized insertion rig (Fig. 2c) with an attached ±25 N force gage (AGF25 N, Mecmesin Ltd, UK) with a resolution of 0.005 N which delivered the stent delivery system at a constant speed of 8 mm/s and was delivered at the start of the flowrate pulse. This delivery speed was within the range of 1–10 mm/s applied by others.[11,15,34,36,42,54] A delivery speed of 5 mm/s corresponds to an approximate speed for delivery by a cardiologist.[34] The catheter delivery system was delivered within each vessel for the following three cases;

Case 1 A static internal arterial pressure of 100 mmHg.

Case 2 Pulsatile flow and pressure as prescribed by Fig. 3, with no cardiac motion.

Case 3 Pulsatile flow and pressure as prescribed by Fig. 3 with cardiac motion as given by Fig. 4a.

The catheter was repeatedly tracked five times for all configuration states.

Numerical Obtained Wall Shear Stress (WSS) Values

The WSS was calculated within Ansys CFX for all coronary vessel geometries as shown in Figs. 1c and 1d.

The Navier–Strokes equations were solved by the finite volume method by applying the second order backward Euler scheme. The inlet and outlet boundary conditions for each vessel were based on the experimentally obtained values as shown in Fig. 3. The fluid was modeled as a Newtonian fluid with a viscosity of 0.004 Pa s. The walls were assumed rigid. The final mesh had over 200,000 tetrahedral elements as generated within the Ansys ICEM module. Grid independence was insured with less than a 2% variation in WSS between mesh densities. Along the cross-section there was a greater density of cells towards the proximal layer with cell sizes in contact with the wall being three times smaller than cells within the center of the flow field for each tested mesh density. Pulse cycle independence was found after the third cycle with a time step size of 0.005 s.

RESULTS

Figure 3 shows the comparison of the *in vitro* replication of the LAD, LCX[13] and RCA[51] flowrate waveforms with a period of 0.83 s. There was a maximum difference of 10.3, 10.8, and 9.3% between the required and measured flow rates within the LAD, LCX and RCA respectively. The pressure pulse for
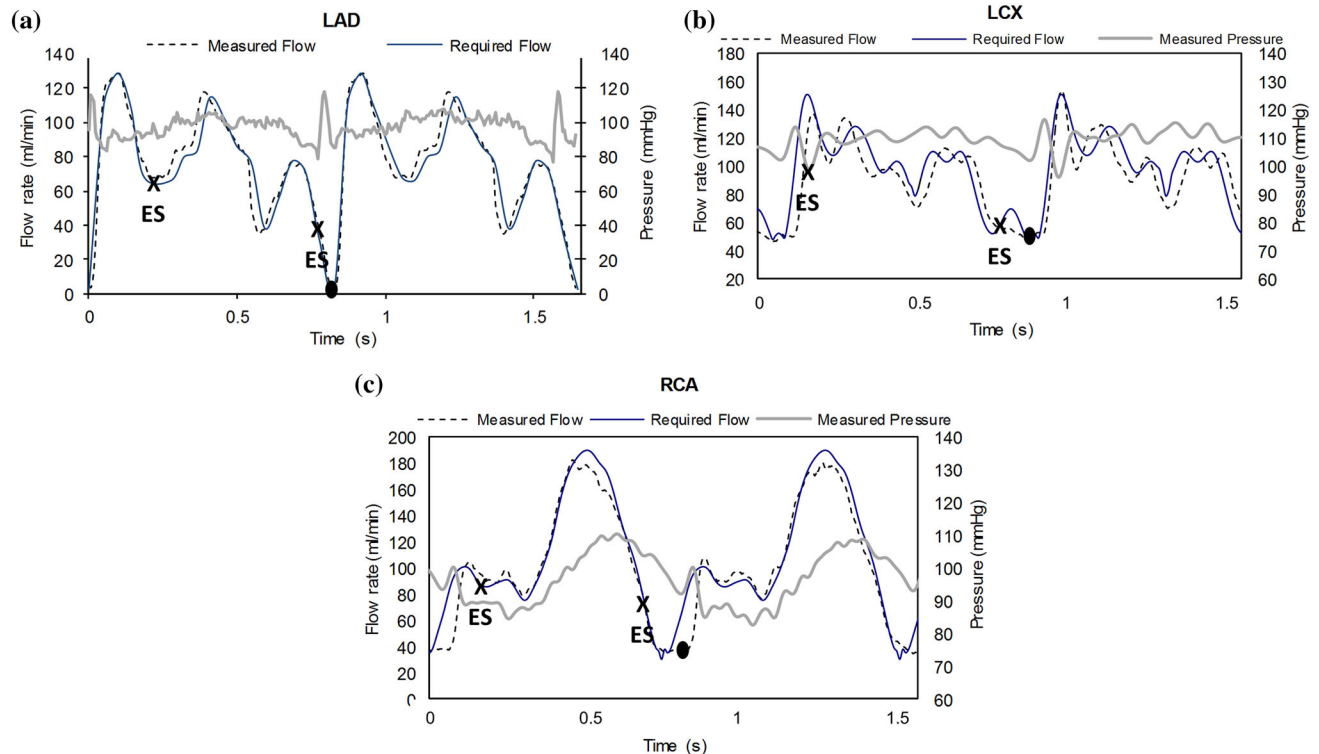

FIGURE 3. Physiological flow rates and pressures for (a) LAD, (b) LCX, and (c) RCA. The filled circle represents the end of the first cycle. End diastolic (ED) and end systolic (ES) are shown by the cross.
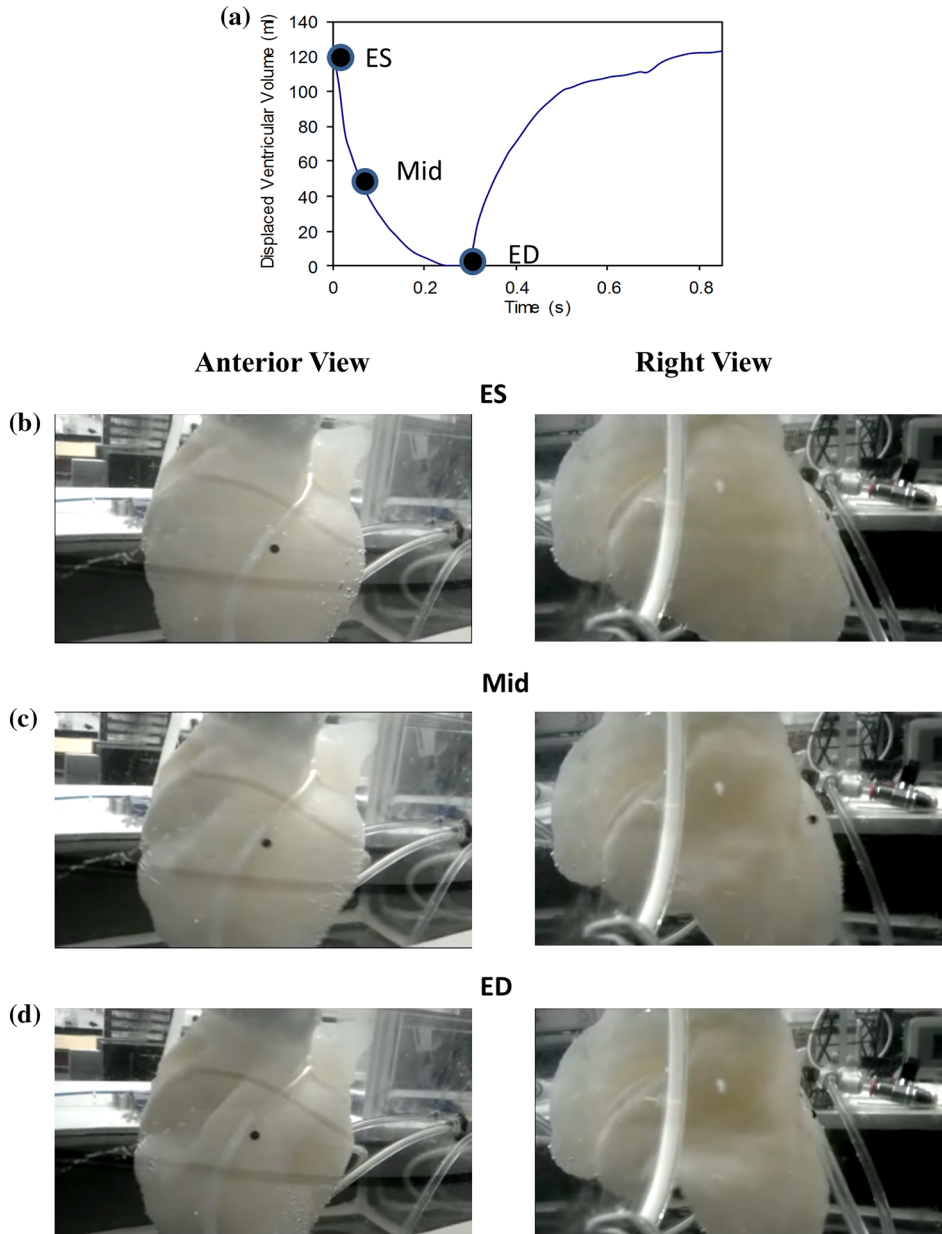
FIGURE 4. (a) Displaced ventricular volume; three phases of the contraction cycle during systole shown for the anterior and right views (b–d). ED is end diastolic, ES is end systolic, and Mid is midway between ED and ES.

each model was within the physiological pressure ranges for all coronary vessels.[44] The corresponding systolic/diastolic pressures in mmHg varied from 118/83, 114/98 and 108/85 for the LAD, LCX and RCA respectively.

Figure 4a shows the physiologically representative stroke volume waveform[10] that was imposed on cardiac phantom. The cardiac motion during three phases of the contraction cycle during systole is shown in Figs. 4b–4d for both the anterior and right views. Figures 5 and 6 shows the outlet flowrates and pressure drops along each vessel's length for all three

vessels with and without cardiac motion. The flowrates and pressure drops for one cardiac cycle are shown in Figs. 5a, 5c, 5e, 6a, 6c, and 6e, respectively while the time-averaged flowrates and pressure drops are shown in Figs. 5b, 5d, 5f, 6b, 6d and 6f respectively. The time-averaged flowrates and pressure drops were calculated by Eqs. (2) and (3) with the results plotted against time as shown in Figs. 5 and 6 to shown the variation over one cardiac cycle

$$\dot{Q}_{avg}(t) = \frac{1}{t} \int_0^t \left(\dot{Q}(t) \right) dt, \qquad (2)$$
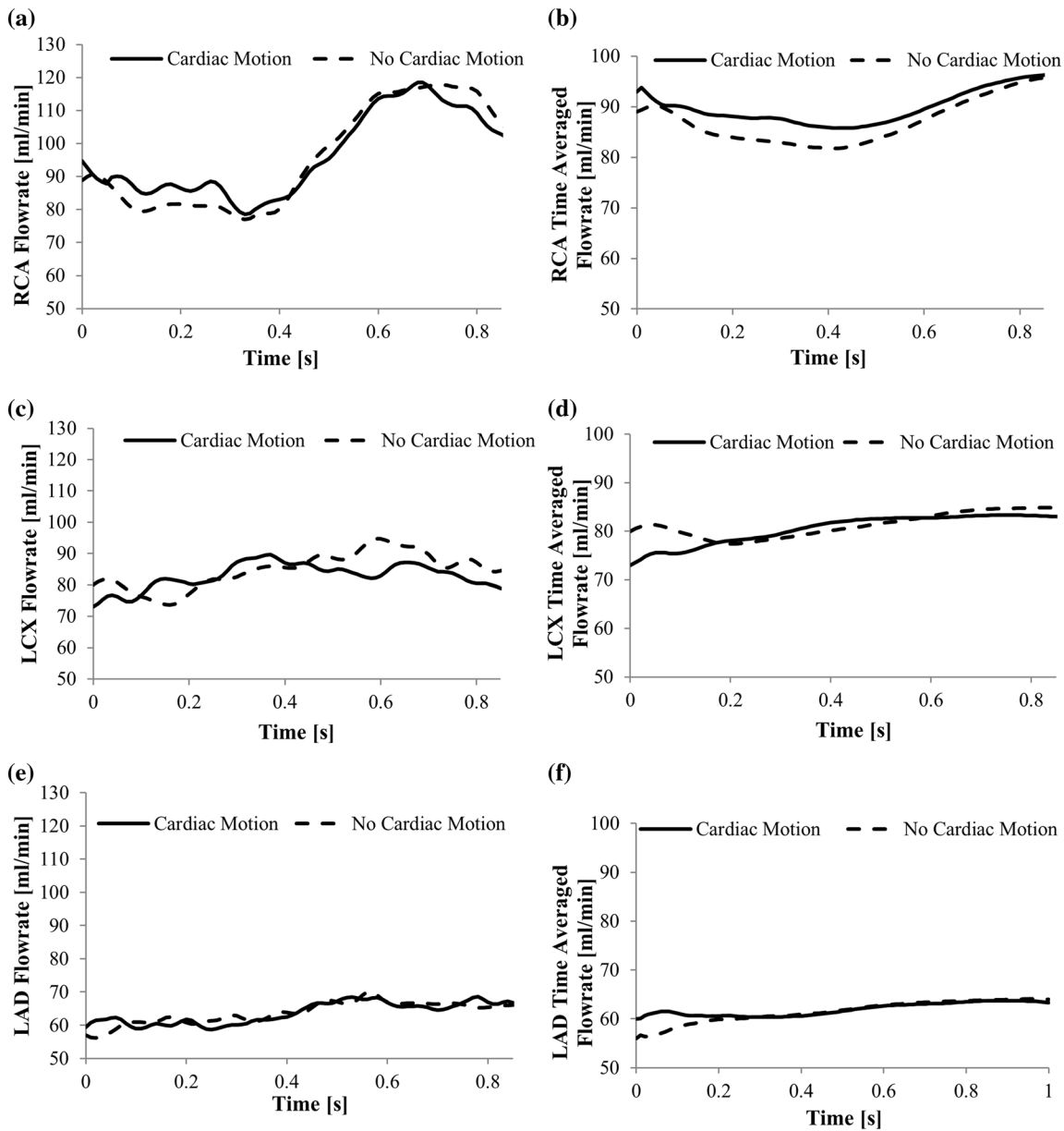
FIGURE 5. The effects of cardiac motion vs. no cardiac motion on outlet and time-averaged flowrates for the RCA (a and b), LCX (c and d), and LAD (e and f).

$$\Delta P_{avg}(t) = \frac{1}{t} \int_0^t (\Delta P(t)) dt. \qquad (3)$$

Table 2 summarizes Figs. 5 and 6 in terms of range, mean and standard deviation. Without cardiac motion the flowrates varied from (77 to 118 mL/min), (56 to 70 mL/min), and (74 to 95 mL/min) for the RCA, LAD, and LCX respectively with slight variations in flowrate ranges occurring with the inclusion of cardiac motion. The corresponding pressure drops as shown in Table 2 for no cardiac motion varied from (2 to

28 mmHg), (−0.9 to 49 mmHg), and (−7.4 to 27 mmHg) for the RCA, LAD, and LCX respectively. While pressure drop changes with cardiac motion varied from (5 to 31 mmHg), (−2 to 45 mmHg), and (−4 to 20 mmHg) for the RCA, LAD, and LCX respectively. The pairwise percentage difference comparison with inclusion of cardiac motion on outlet flowrates and pressure drops are given in Table 3. The negative and positive sign given in Table 3 indicates that the cardiac motion either decreased or increased the % difference values respectively. This pairwise comparison showed less than a 4% and up to 30%
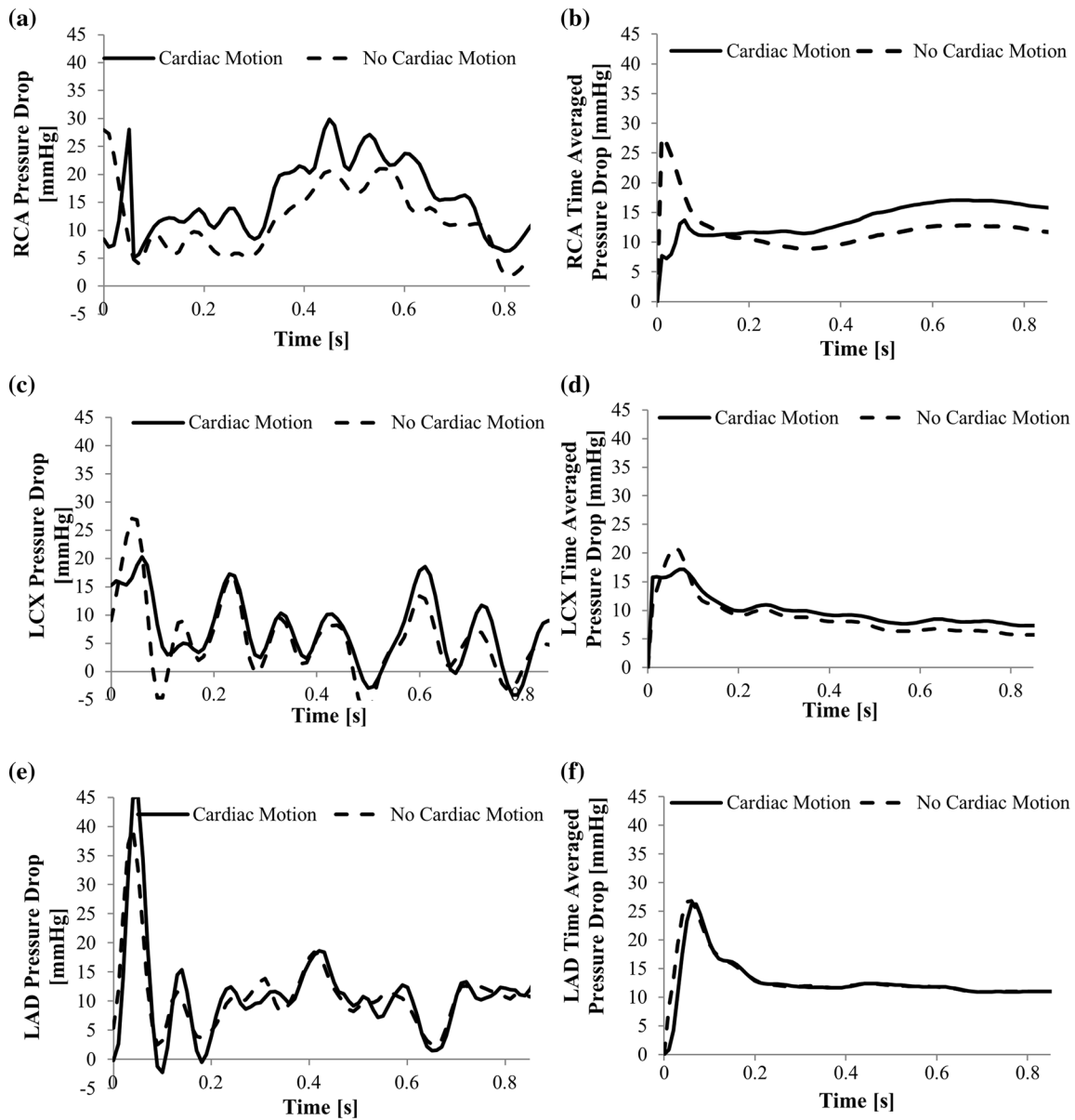
FIGURE 6. The effects of cardiac motion vs. no cardiac motion on the pressure drop and time-averaged pressure drops along the coronary vessels for the RCA (a and b), LCX (c and d), and LAD (e and f).

TABLE 2. The mean and range values for the outlet flowrates and pressure drops occurring along the RCA, LAD, and LCX vessels with/without cardiac motion.

| | Without cardiac motion | | | | With cardiac motion | | | |
| | Outlet flowrate (mL/min) | | Pressure drop (mmHg) | | Outlet flowrate (mL/min) | | Pressure drop (mmHg) | |
Vessel	Range	Mean ± SD	Range	Mean ± SD	Range	Mean ± SD	Range	Mean ± SD
RCA	77.0–117.8	95.6 ± 14.4	1.8 to 28.0	12.1 ± 6.4	78.6–118.5	95.8 ± 11.8	5.1 to 31.2	15.7 ± 6.8
LAD	56.2–70.0	63.9 ± 3.1	−0.9 to 39.7	10.0 ± 6.4	54.6–68.6	63.3 ± 3.4	−2.2 to 45	10.23 ± 7.7
LCX	73.7–94.7	84.4 ± 5.3	−7.4 to 27.1	5.3 ± 6.3	73.0–89.6	82.2 ± 4.1	−4.2 to 20.31	6.9 ± 5.9

mean variation between the outlet flowrates and pressure drops respectively. This suggests that pressure drop variation is more sensitive to cardiac motion than outlet flowrates as can be seen by the interquartile range values (Table 3).

To assess if there were any significant difference due to the inclusion of cardiac motion on outlet flowrates and pressure drops over one cardiac cycle, the non-parametric Mann–Whitney pairwise comparison at the 95% confidence interval (CI) was conducted within the statistical software MINITAB 16.2.0 (State College, PA, USA) (Table 4) and was confirmed by the Krushkal-Wallis test. P values of <0.05 were deemed significant. The negative and positive sign indicates that the cardiac motion either decreased or increased the values respectively as shown in Table 4. The percentage variation in CI is given in the round brackets. The cardiac motion had a significant difference on outlet flowrates for the LCX vessel ($p = 0.002$) during one cardiac cycle, with no significant difference found for the RCA and LAD vessels ($p > 0.08$). While the cardiac motion significantly changed ($p < 0.009$) the pressure drops for two out of the three vessels (RCA and LCX).

The pressure drop along the varying degrees of stenosis is shown in Fig. 7 for the steady flow (Fig. 7a) and the time-averaged (Fig. 7b) and maximum pressure drop (Fig. 7c) conditions. Figure 7a also shows

the superimposed time-averaged and maximum pressure drop pulsatile flow on the steady flow conditions which agreed with the steady pressure drop measurements. The pressure drop measurements shown in Fig. 7 correspond to the pressure drop occurring across the stenosis. This pressure drop across the stenosis was found by subtracting the pressure drop measurement across the stenosis vessel from an unblocked vessel. The time-averaged pressure drop with a Reynolds number of 110 varied from 2.5 mmHg (56% area occlusion) to 13.4 mmHg (89% area occlusion) while the maximum pulsatile pressure drop with a Reynolds number of 313 varied from 7 to 49 mmHg. The pressure drops varied in a quadratic trend ($r^2 > 0.99$) for the steady flowrates (Fig. 7a) which agree with the findings of Steinman *et al.*[41] for a stenosis within a giant intracranial aneurysm. For the three percentage stenosis area reductions, the pressure drop varied in an exponential manner which follows a similar non-linear trend found by Kamangar *et al.*[14] There was no noticeable difference in pressure drop across the stenosis with the inclusion of cardiac motion.

The average trackability forces (F_T) of the five tests for delivering the coronary stent delivery system within the RCA, LAD, and LCX hydrogel models are shown in Figs. 8a–8c for all three tested scenarios with the superimposed centreline curvature. For the static

TABLE 3. Pairwise percentage difference comparison of outlet flowrates and pressure drops for simulations with cardiac motion vs. without cardiac motion.

| | % pairwise comparison—with cardiac motion vs. without cardiac motion | | | | | |
| | Outlet flowrate | | | Pressure drop | | |
Vessel	IQR	Mean	SD	IQR	Mean	SD
RCA	−2.7, +4.3	−0.9	4.2	−17.3, +39.9	+29.9	57.2
LAD	−3.2, +0.9	−1.4	3.7	−11.9, +20.2	+6.8	396.2
LCX	−6.3, +1.4	−3.9	5.7	+5.8, +52.9	+26.4	224.2

A positive or negative sign refers to an increase or decrease in percentage difference respectively. IQR refers to interquartile range at the 25th and 75th percentile. SD refers to standard deviation.

TABLE 4. Pairwise comparison of the outlet flowrates and pressure drops based on the Mann–Whitney method at the 95% confidence interval (CI).

| | Pairwise comparison—cardiac motion vs. no cardiac motion | | | | | |
| | RCA | | LAD | | LCX | |
Vessel	CI	p value	CI	p value	CI	p value
Flowrate (mL/min)	−2.450, +4.790, (−2.6, +5.3)	0.2205	−1.429, +0.211 (−2.2, +0.03)	0.0861	−3.652, −0.722 −4.06, −0.90	0.0018
Pressure drop (mmHg)	+1.612, +5.318 (+14.4, +47.7)	0.0002	−0.854, +1.370 (−8.5, +13.6)	0.3333	+0.329, +3.373 (+8.06, +82.6)	0.0089

p values <0.05 were deemed significant. A positive or negative sign refers to an increase or decrease in value respectively. Percentage variations are given within the round brackets.
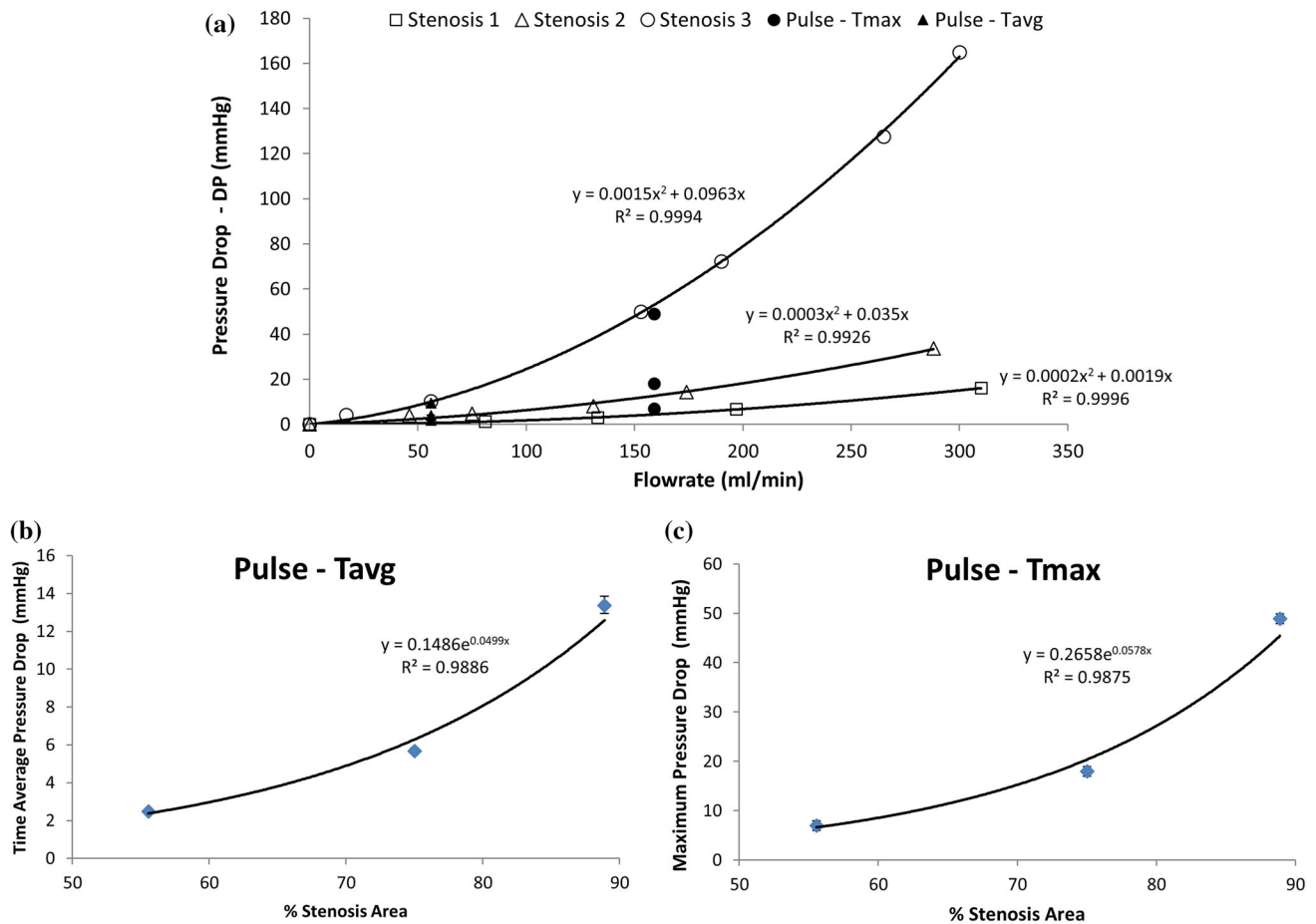
FIGURE 7. The measured pressure drops based on the RCA waveform across the three sized stenosis for (a) steady flow with superimposed maximum and time-averaged pressure drops, (b) time-averaged pulsatile pressure drop, and (c) maximum pulsatile pressure drop.

scenario (Case 1) the trackability forces ranged from (0.238 to 0.851 N), (0.329 to 0.784 N), and (0.454 to 0.626 N) for the RCA, LAD, and LCX respectively, while with the inclusion of pulsatile flow and cardiac motion (Case 3) the trackability forces ranged from (0.467 to 0.823 N), (0.309 to 0.773 N), and (0.419 to 0.871 N) for the RCA, LAD, and LCX respectively (Table 5). Table 6 summarizes the main percentage differences between all three cases with maximum and average percentage differences of (23–56%) and (0.3–11%) respectively with standard deviations of (5–16%). To assess if there was a significant difference in trackability forces between all three scenarios along the three vessel paths, the non-parametric Mann–Whitney pairwise comparison at the 95% confidence interval (CI) was conducted within the statistical software MINITAB 16.2.0 (State College, PA, USA) (Table 7). There was a significant difference for all pairwise comparisons ($p < 0.0001$).

A correlation analysis was conducted between the centreline curvature and the trackability forces for all vessels over the entire length of each model as shown in Figs. 9a–9c. To further investigate, if a correlation exists between the data sets, the cumulative trackability force ($F_{CT}(l)$) (Eq. 4) and the cumulative curvature ($k_C(l)$) (Eq. 5) was obtained by integrating the trackability force and curvature along the vessel's length (l) and plotted against each other as shown in Figs. 9d–9f

$$F_{CT}(l) = \int_0^l F_T(l)dl \qquad (4)$$

$$k_{CT}(l) = \int_0^l k_T(l)dl. \qquad (5)$$

As shown in Figs. 9d–9f, there was a good correlation between the cumulative trackability force and the cumulative curvature with R^2 values of 0.9744, 0.9912, and 0.9665 for the LAD, LCX, and RCA respectively. Furthermore, the slopes of each line were quite similar
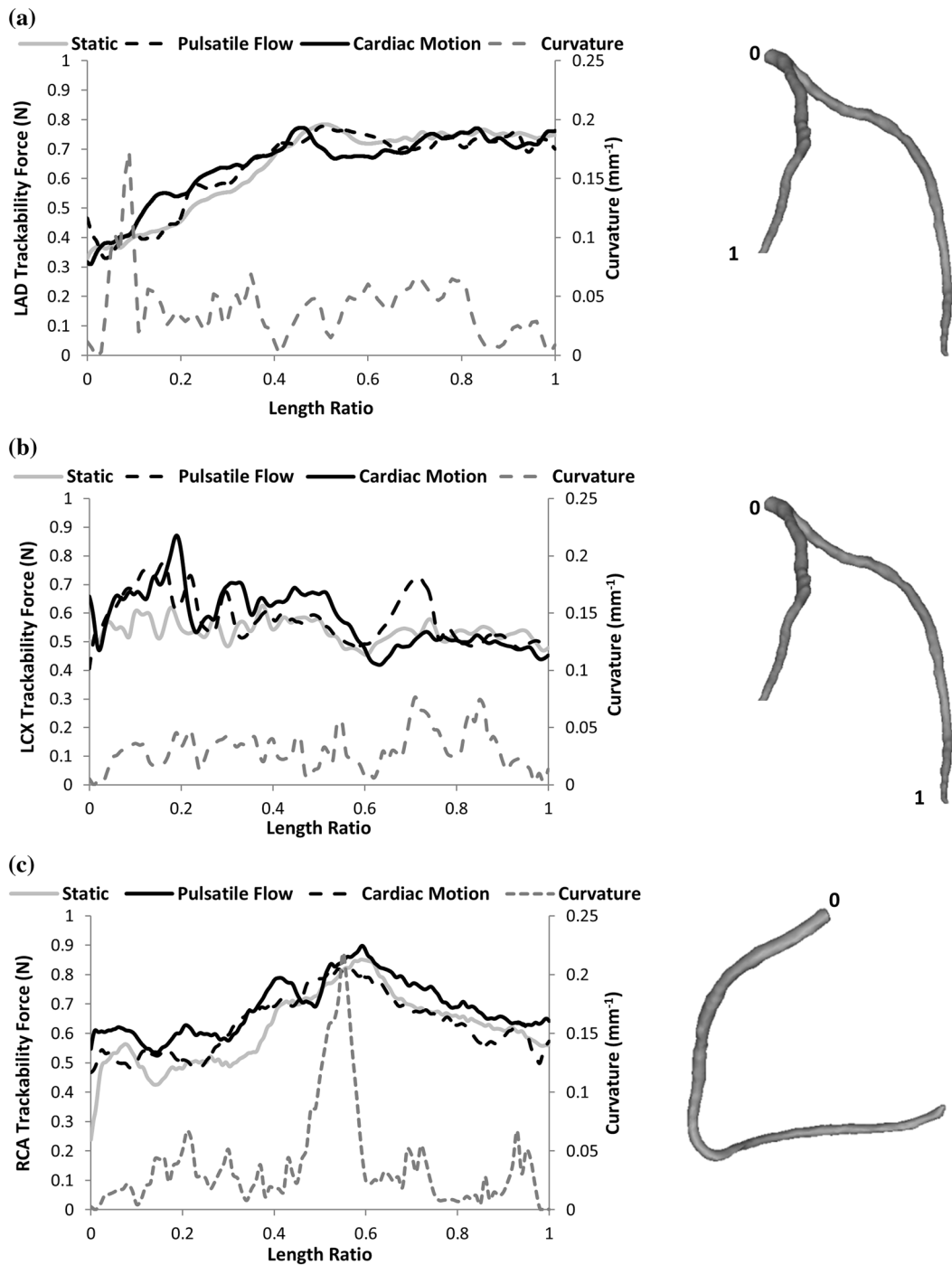
FIGURE 8. The curvature and trackability forces along the length for the for the static, pulsatile flow and cardiac motion cases in (a) LAD, (b) LCX, and (c) RCA.

with values of 0.9, 0.6, and 0.4×10^{-3} mm/N for the LAD, LCX, and RCA models respectively.

A 1 mm diameter catheter was delivered across the three sized stenosis to assess the catheter pushability forces required to cross a stenosis. There was no noticeable increase in force for the 56 and 75% area

stenosis while a force of 2.7 N was obtained to cross the 89% stenosis.

The WSS values at maximum velocity along the outer wall are shown in Fig. 10. The WSS values were the same circumfentially along all models except at regions of high curvatures which occurred at a length

TABLE 5. The trackability force values in Newtons for all three scenarios occurring within the RCA, LAD, and LCX vessels.

	Vessel					
	RCA		LAD		LCX	
Scenario	Range	Mean ± SD	Range	Mean ± SD	Range	Mean ± SD
Case 1	0.238–0.851	0.618 ± 0.119	0.329–0.784	0.639 ± 0.036	0.454–0.626	0.538 ± 0.014
Case 2	0.535–0.898	0.688 ± 0.093	0.329–0.777	0.639 ± 0.063	0.406–0.775	0.580 ± 0.013
Case 3	0.467–0.823	0.632 ± 0.101	0.309–0.773	0.647 ± 0.080	0.419–0.871	0.580 ± 0.115

Case 1 is for static pressure only, Case 2 is for pulsatile flow and pressure only, and Case 3 is for pulsatile flow/pressure and cardiac motion.

TABLE 6. The pairwise percentage difference comparison of trackability forces for all three cases.

	% difference—pairwise comparison								
	Case 2 vs. Case 1			Case 3 vs. Case 1			Case 3 vs. Case 2		
Vessel	Maximum	Average	SD	Maximum	Average	SD	Maximum	Average	SD
LAD	+29.4	+0.3	5.4	+22.6	+1.9	9.2	−47.3	+1.4	9.9
LCX	+32.8	+5.9	10.9	+34.6	+5.2	13.0	−44.5	−1.6	16.0
RCA	+56.5	+10.7	7.8	+49.0	+2.3	9.8	−27.0	−9.7	8.4

A positive or negative sign refers to an increase or decrease in percentage difference respectively. SD refers to standard deviation. Case 1 is for static pressure only, Case 2 is for pulsatile flow and pressure only and Case 3 is for pulsatile flow/pressure and cardiac motion.

TABLE 7. Pairwise comparison of the trackability forces in Newtons based on the Mann–Whitney method at the 95% confidence interval (CI).

	Pairwise comparison					
	Case 1 vs. Case 2		Case 1 vs. Case 3		Case 2 vs. Case 3	
Vessel	CI	*p* value	CI	*p* value	CI	*p* value
LAD	+0.01009, +0.01406 (+1.4, +1.9)	<0.0001	+0.01230, +0.01772 (+1.7, +2.4)	<0.0001	+0.00485, +0.01019 (+0.7, +1.4)	<0.0001
LCX	−0.02860, −0.02474 (−5.3, −4.6)	<0.0001	−0.03692, −0.02995 (−6.9, −5.6)	<0.0001	+0.00346, +0.00822 (+0.6, +1.5)	<0.0001
RCA	−0.07579, −0.06987 (−12.3, −11.3)	<0.0001	−0.01583, −0.00978 (−2.6, −1.6)	<0.0001	+0.05692, +0.06234 (+8.4, +9.2)	<0.0001

p values <0.05 were deemed significant. A positive or negative sign refers to an increase or decrease in value respectively. Percentage variations are given within the round brackets.

ratios of 0.75–0.85 and 0.85–1 for the RCA and LCX respectively. For these two locations there was an average of 2- and 1.2-fold increase in the outer wall WSS when compared with the inner wall. The numerically obtained WSS values were correlated with experimentally found trackability forces of Case 1 with a positive linear relationship shown for the RCA and LAD (Figs. 10b and 10c) and a negative linear relationship for the LCX (Fig. 10c).

DISCUSSION

In vitro vascular models are an attractive platform for hemodynamic assessment for understanding hemodynamic parameters and validating numerical simulations and preclinical device testing with most medical device companies evaluating their stent delivery systems along curved pathways.[2] Previous *in vitro* coronary trackability studies were conducted in two-dimensional rigid pathways with unspecified co-efficient of friction values.[11,15,34,36,42,54] Also, these studies were not based on patient-specific geometries. Previous *in vitro* studies have excluded the effects of pulsatile flow/pressure and cardiac motion on the coronary vasculature. As far as the authors are aware this is the first hemodynamic and catheter trackability study which experimentally examined various hemodynamic parameters within healthy/diseased cases and delivered a coronary stent delivery system within a thin-walled
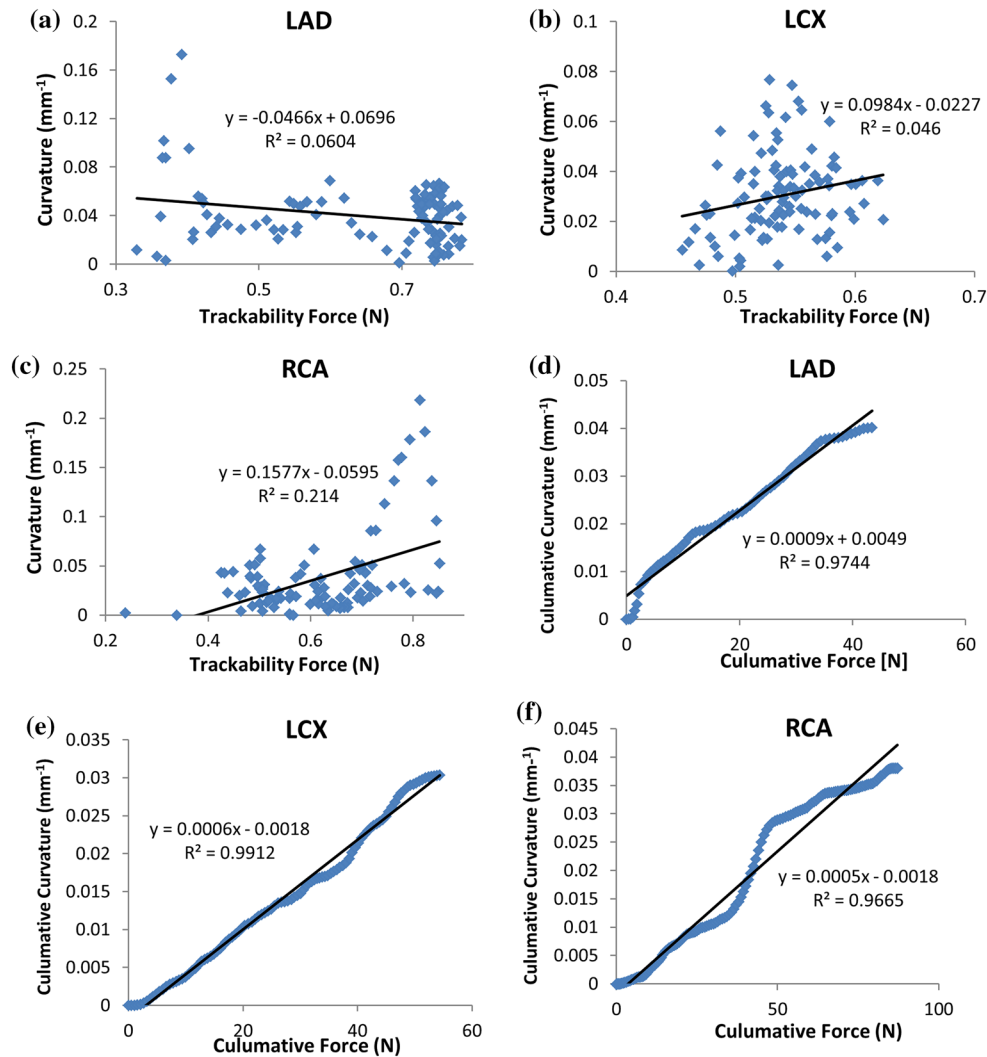
FIGURE 9. A correlation of curvature against trackability forces (a) RCA, (b) LAD, and (c) LCX; a correlation of cumulative curvature against cumulative trackability forces (d) RCA, (e) LAD, and (f) LCX.

flexible patient-specific coronary phantom models supported within the heart grooves of a dynamic cardiac phantom which replicating the arterial's co-efficient of friction values. This study assessed the influence that pulsatile flow and cardiac motion may have on the hemodynamics and trackability forces.

The cardiac simulator produced excellent cycle-to-cycle flowrate repeatability which followed the complex shape of the coronary flowrates. The pressure was within physiological upper and lower limits and can be controlled by varying the outlet valve resistance and incorporating an air chamber downstream of the phantom models. The pressure within the coronary vessels is much more out of phase when compared to other vessels within the cardiovascular system as the maximum flowrate occurs during the diastolic phase, while maximum pressure occurs during the systolic phase.[7,25] This out of phase phenomenon cannot be

replicated by our current cardiac simulator. This would be resolved by incorporating a programmable outlet valve which would vary the outlet resistance during the cardiac cycle thus replicating coronary blood pressure accurately. Analyzing the video evidence as shown in Fig. 4, the cardiac motion has a non-homogenous deformation with the largest deformation occurring mid-way between the base and apex of the heart which is similar to the *in vivo* measurements within canines[40] and healthy adults.[3] Bogaert and Rademakers[3] observed by magnetic resonance myocardial tagging that the left ventricular wall flattens towards the apex similar to observed dynamic deformation of our cardiac phantom.

Simplifications to the modeling process are desirable due to the cost involved in replicating cardiac muscle motion with coronary flowrates. The contraction and expansion of the cardiac muscle generates large dis-
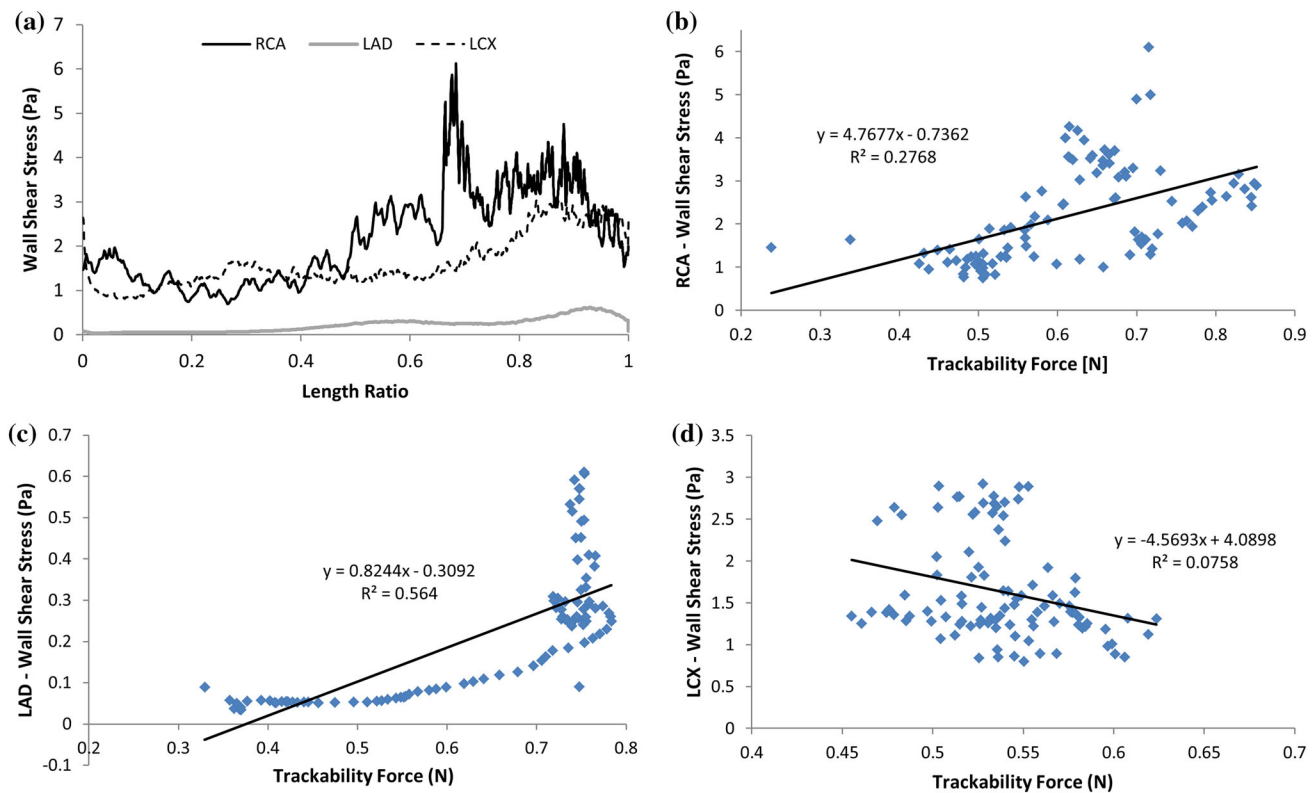
FIGURE 10. (a) Computationally obtained wall shear stress (WSS) values, correlation of WSS values with trackability forces for (b) RCA, (c) LAD, and (d) LCX. WSS values were obtained at maximum velocity occurring at a time of 0.05, 0.09 and 0.16 s for the RCX, LAD, and LCX respectively.

placements within the coronary arterial tree. Others have assessed numerically the impact of moving wall boundaries within the aorta,[9,19,29,37,38] carotids,[30,52] and coronaries[16,31,32,45,51] on arterial hemodynamics. Ene *et al.*[9] concluded that moving wall boundaries are required for assessing flow patterns and wall shear stress patterns while static pressure conditions were sufficient for assessing von misses stress within the arterial wall. Our study found that the outlet flowrates was significantly affected throughout the pulse cycle within the LCX ($p = 0.0018$), while small temporal variations occurred along the length for all three vessels. Cardiac motion significantly affected the pressure drop for the RCA and LCX ($p < 0.009$) with mean increases of 30 and 26% for the RCA and LCX vessels respectively. The RCA and LCX are both located on the arterio-ventricular grooves. These arteries are subjected to cardiac muscle compressions and distortions. The LAD had a very similar trend in magnitude and shape for the simulation with and without cardiac motion with a lower mean increase of 6% and no significant difference in pressure drop during one pulse cycle ($p = 0.33$). The LAD is not as susceptible to the motion of the ventricle as the other two vessels as it is located on the thick walled septum between the two

ventricles which prevents much of the arterial constriction. This finding is in agreement with X-ray coronary angiography data which found lower displacements occurring for the LAD when compared with the LCX.[53] Others have shown that the phasic relation between the flow rates and arterial wall dynamics caused by coronary wall motion significantly influences the temporal variations in wall shear stress and flow patterns[31,32,45,51] while the time-averaged wall shear stress was not appreciably affected.[51] This is in agreement with our findings for outlet flowrates, with no noticeable changes in time-averaged outlet flowrates for the LAD and LCX vessels. Kolandavel *et al.*[16] found that coronary wall motion altered the time-averaged species transport process of oxygen and low-density lipoproteins within coronary vessels.

The pressure drop can affect the fractional flow reserve by impeding oxygen delivery to the heart muscle, with higher flowrates and increased stenotic areas generating a non-linear increase response in pressure drops. Our pressure drop measurements are within the range calculated numerically and invasively measured trans-stenotic pressure drops across 21 left/right coronary vessels within 19 patients by Kousera *et al.*[17] Their pressure drops varied approximately from 5 to

27 mmHg for a stenosis percentage areas of 66 ± 12, diameter of 2.45 ± 0.59, length of 16.00 ± 8.19 mm and Reynolds number of <400. Also our findings agree with the numerically obtained pressure drops of Kamangar et al.[14] who simulated coronary waveforms within idealized straight stenosis models of varying lesion geometries. They found pressure drop variations of 4.8–45 mmHg for a percentage area stenoses of 70–90% with 10 mm lesion lengths.

Trackability describes the deliverability of a stent system along a curved vessel up to the lesion.[36] The higher the trackability force, the greater force the physician will have to exert to track the device to the required location. Our results agreed with previous two-dimensional trackability studies conducted by Rieu et al.[34] and Schmidt et al.,[36] who found variations in median trackability forces of 0.24–1.34 N for seventeen coronary stent delivery systems and maximum trackability forces of 0.35–0.6 N for five commercially available stent delivery systems respectively. Rieu et al.[34] conducted trackability tests along a 3 mm inner diameter two-dimensional pathway comprising of two bends of 90° (curvature of 0.1 mm^{-1}) and 135° (curvature of 0.2 mm^{-1}) within paraffin oil while Schmidt et al.[36] delivered the devices within a constant diameter rigid high-density polyethylene tubing of 2.5 mm inner diameter comprising of two bends with curvatures of 0.1 mm^{-1} along the same two-dimensional plane. These curvature variations were within the range of our three patient-specific models. Also our results agreed with Fedel et al.[11] who delivered 25 rapid exchange PTCA catheters from various manufactures along a three-dimensional rigid tube pathway. They obtained a trackability force measurement ranging from 0.4 to 0.85 N. The heart grooves within our cardiac model provided a rigid anchorage for all three vessels and this may explain the agreement with previous two-dimensional trackability studies within rigid pathways. The three-dimensional nature of our vessels did not influence the maximum trackability forces.

The RCA vessel had a sharp increase in curvature occurring at a length ratio of 0.55 due to the sharp bend which had a highest overall curvature. This increased curvature lead to a corresponding increase in trackability force. It was difficult to assess the impact of curvature for the other two models on trackability forces. At the entrance to the LAD vessel there was a steep increase in curvature with no direct increased spike in trackability force. The arterial diameter at the LAD entrance was 45% larger than that of the RAC at a length ratio of 0.55 and 88% larger than the delivery catheter. This increased size in diameter at the entrance may explain why there was no correlation in curvature with the trackability force as the catheter would not travel along the centreline but rather along a straight

line path. For low curvature values of <0.1 mm^{-1} within vessels approaching the size of the catheter there is no obvious correlation trend as was the case for the LAD and LCX vessels. This lack of correlation for the LAD and LCX ($R^2 < 0.06$) is further shown in Figs. 9a and 9b, with a positive linear correlation for the RCA vessel (Fig. 9c—$R^2 = 0.21$). However, by correlating the cumulative trackability force with the cumulative curvature provided a strong positive linear correlation. These cumulative values were obtained by integrating the values along the vessel's centreline with slopes varying from 5 to 9×10^{-3} m^{-1}. These cumulative values have the advantage of including the vessel in contact with the delivery catheter which may be used to predict trackability forces along known coronary geometries. If successfully proven using larger populations, cumulative curvature could be used as a predictive clinical tool to aid stent delivery to the lesion vicinity, by deciding upon the most appropriate catheter design option.

The question as to whether these large displacements affect trackabilty forces during catheter delivery was assessed. With the inclusion of the pulsatile flow and cardiac motion simulations (Case 3), there were maximum variations in trackability forces of 23, 35, and 49% for the LAD, LCX, and RCA vessels respectively for the static pressure scenario (Case 1) and 47, 45, and 27% for the LAD, LCX and RCA vessels respectively for the pulsatile flow scenario (Case 2), with average percentage variations of 2–5% and 1–10% for Case 1 and Case 2 respectively (Fig. 8; Table 6). Referring to Fig. 8, the trackability forces increase along the length from a length ratio of 0–0.6 for the RCA and LAD, while the LCX oscillated for the first 20% of the vessel. As observed by the video evidence, the catheter shaft was continuously in contact with the arterial wall at multiple contact points that varied along the course of delivery. This contributed to the trends shown in trackability forces.

There was a significant difference between all pairwise comparisons ($p < 0.0001$) as shown in Table 7. The lowest variation in trackability forces occurred along the LAD for Cases 1 and 2 when compared with Case 3, with confidence interval variations of $<2.4\%$. While increased confidence interval variations of 0.6–6.9 and 1.6–12.3% occurred for the LCX and RCA respectively. The LAD sits on the septum between the right and left ventricles which protects it from much of the ventricle motion. This may explain this reduced variation in trackability forces along the LAD vessel. The RCA and LCX arteries are subjected to arterial constriction as these vessels are attached between the ventricles and atriums with less protection from the contracting chambers. When compared with the full cardiac motion with pulsatile flow (Case 3) along the

vessel's length the Mann–Whitney analysis showed on average the static simulation (Case 1) was lower than the trackability forces within the LCX and RCA vessels while the pulsatile flow with no cardiac motion (Case 2) was on average higher for all three vessels along the vessel's length. Along the vessel's length, point variations occurred. Case 3 was higher at particular locations within the LAD (length ratio: 0.1–0.3 and 0.45) and LCX (length ratio: 0.2 and 0.3–0.6), while Case 2 was higher in other locations along the RCA (length ratio: 0–0.45 and 0.5–1), LCX (length ratio: 0.6–0.75). There was no difference between all cases along the LAD length except for two locations at length ratios of 0.1 and 0.5. The maximum difference between the three cases occurred within the LAD at length ratios of 0.15 occurring during the acceleration phase of the pulse cycle and during end diastolic, LCX at length ratios of 0.2 occurring during the deceleration phase of the pulse cycle and during end systolic and RCA at a length ratio of 0.2 occurring at the start of the flowrate cycle and during the ventricular expansion. These maximum variations occurred during different times of the flowrate and cardiac motion cycle. Also, these findings may be explained by the fact that during cardiac motion (Case 3) the radius of curvature for the all vessels changed. The cardiac motion may have increased the radius of curvature by flattening both ventricles as well as increasing the resistance to the advancing catheter.

The WSS was considerable higher for the RCA vessel. This was due to the larger curvature occurring at mid-length which skewed the blood flow towards the outer wall. Also the RCA had the greatest fluctuations in WSS along the length which was caused by greater fluctuations in centreline curvature and an increase in maximum RCA velocity of 46 and 26% when compared with the LAD and LCX respectively. There was a week linear positive trend in WSS and trackability forces for the RCA and LCA vessels (Figs. 10b and 10c) and a week linear negative trend for the LCX vessel (Fig. 10d). Regions of high WSS values did not directly correlate to the peak trackability forces. The time-averaged WSS for the LAD and LCX was less than 1.5 and 0.25 Pa respectively. This was due to the relatively straight vessels of the LAD and LCX when compared with the RCA.

The pushability of a delivery catheter across a stenosis can increase the delivery forces depending on the area reduction and stenosis compliance.[15] Schmidt et al.,[36] found no noticeable increase in force across a stenosis which agrees with our findings for the 56 and 75% area stenosis, while there was threefold increase in force for delivering across the 89% stenosis when compared to the trackability forces, due to the compression of the stenosis against the advancing catheter.

Kinney et al.[15] found pushability forces of 0.5–2 and 1.5–8 N for compliant and less compliant stenosis. They experimentally delivered catheters of diameters 2.3–4.0 mm within a 6 mm rigid tube comprising of an 80% diameter reduction. Care is required in advancing catheters through small openings so as not to damage the advancing catheter. The torquability of a catheter is important for navigating through tight curvatures and cross various sized stenosis. The construction of the catheter shaft must allow the physician to easily twist the catheter with a very close to one-to-one torque ratio between the proximal end and distal tip. This one-to-one torque ratio will also provide better distal tip positioning and facilitate easier arterial navigation. Further device improvements in reducing trackability and pushability forces includes selecting a low friction outer layer or coating, reducing the stiffness, wall thickness, outer diameter and distal tip profile. Reducing the catheter profile and stiffness may assist in reducing delivery forces but could comprise kink resistance due to a weaker catheter structure. Also, increased lubricity may create a false lumen as the catheter could easily be pushed between the stenosis and arterial wall. All of these design changes need to be tested within various sized stenosis and vessel curvature to provide the best optimized solution.

Sharper angulations result in greater shear forces during advancement of a given catheter. Excessive shear forces may result in intimal tearing or dissection, rendering the vessel susceptible to thrombosis. There is often a delayed manifestation of these injuries, with the possibility that catheter induced injuries are not attributed to the catheter delivery path.[15] Mechanical damage to biological tissues occurs when the shear stress reaches a critical value. Kinney et al.[15] showed that shear forces of 3 ± 1.9 and 16.7 ± 6.8 N are required to cause dissection and perforation within 48 iliac and femoral necropsy samples. Even though these results are for a larger sized vessels, it provides a guideline in the absent of similar studies within coronary sized vessels. The trackability forces recorded within our phantom models were much lower than those reported forces required to cause tissue damage and therefore it would be unlikely that tissue damage would occur during the advancement of a stent delivery system within coronary vessels with a maximum curvature of 0.22 mm^{-1}, under dynamic flow and cardiac motion. From our CFD simulations high WSS values were found in excess of 3 Pa for the RCA and LCX vessels. These high WSS values can induce apoptosis of smooth muscle cells which can enhance plaque vulnerability.[35]

There were several limitations to this study. The analysis was completed using three coronary vessels from one patient-specific cardiac model, which is not a

full representation of a larger population. A resting ventricular volume loading and heart rate was simulated. Exercise conditions may further affect the findings within this study. Unfortunately, due to the acceleration limit on the linear actuator, higher cardiac stroke volumes and exercise pulses were not simulated within the current setup. To overcome this limitation larger sized piston bores will be incorporated to facilitate future testing. These coronary waveforms have multiple acceleration and deceleration phases during one cardiac cycle which resulted in noisy pressure waveforms as was the case for the LCX and to a lesser degree the LAD. During testing there were less than a 5% variation in mean blood pressure between all cycles. The insertion of the catheter was delivered at the start of the flowrate waveforms. Further tests are required to assess if insertion during different stages of the pulse cycle affects trackability forces. Only one type of stent delivery system was tested in this study. Different delivery systems may produce different trackability forces within the same vasculature. Rieu *et al.*[34] and Schmidt *et al.*[36] and found variations in trackability forces of (0.35–0.62 N) and (0.4–1.4 N) respectively within the same pathways for a number of commercially available stent delivery systems. Although variations do exist from one stent delivery type to another it, the authors would not expect that this would affect the outcome of our study in showing the differences between the three different cases. The numerically obtained WSS values were simulated by approximating the walls to be rigid. This can underestimate the WSS values by as much as 10–25% when modeling the wall as compliant as found previously for smaller sized vessels[20,30,52] and 5% difference for time-averaged WSS values.[20] Malve *et al.*[20] found similar trends in the temporal maximum and minimum WSS values along the bifurcation of the left coronary artery when comparing rigid wall CFD with compliant wall FSI.

CONCLUSION

A patient-specific cardiac test facility was designed and developed which can produce reproducible results and facilitates a better understanding of the interaction between geometrical parameters, physiological conditions and trackability forces. It was found that pressure drop variations are more sensitive to cardiac motion than outlet flowrates. Maximum pressure drops varied from 7 to 49 mmHg for a stenosis % area reduction of 56 to 90%, varying in a quadratic trend for varying flowrates and an exponential trend for % area reductions. There was a strong positive linear correlation of cumulative trackability force with the cumulative curvature. When compared to other two-dimensional trackability studies, the three-dimensional nature of the vessels did not influence the maximum trackability forces as the heart grooves provided a rigid anchorage for all three tested vessels. The inclusion of cardiac motion with pulsatile flow significantly altered the trackability forces along the delivery pathways with high local percentage variations.

CONFLICT OF INTEREST

The authors declare that they have no conflict of interest.

HUMAN AND ANIMAL STUDIES

No human or animal studies were carried out by the authors for this article.

REFERENCES

[1]Alfonso, F., C. Macaya, J. Goicolea, R. Hernandez, J. Segovia, J. Zamorano, *et al.* Determinants of coronary compliance in patients with coronary artery disease: an intravascular ultrasound study. *J. Am. Coll. Cardiol.* 23(4): 879–884, 1994.
[2]Balcon, R. Recommendations on stent manufacture, implantation and utilisation. *Eur. Heart J.* 18(10):1536–1547, 1997.
[3]Bogaert, J., and F. E. Rademakers. Regional nonuniformity of normal adult human left ventricle. *Am. J. Physiol. Heart Circ. Physiol.* 280:H610–H620, 2001.
[4]Caldwell, R. A., J. E. Woodell, S. P. Ho, S. W. Shalaby, T. Boland, E. M. Langan, *et al.* *In vitro* evaluation of phosphonylated low-density polyethylene for vascular applications. *J. Biomed. Mater. Res.* 62(4):514–524, 2002.
[5]Capron, L., and P. Bruneval. Influence of applied stress on mitotic response of arteries to injury with a balloon catheter: quantitative study in rat thoracic aorta. *Cardiovasc. Res.* 23(11):941–948, 1989.
[6]Chen, S. Y., and J. D. Carroll. Kinematic and deformation analysis of 4-D coronary arterial trees reconstructed from cine angiograms. *IEEE Trans. Med. Imaging* 21(6):710–721, 2003.
[7]Davies, J. E., Z. I. Whinnett, D. P. Francis, C. H. Manisty, J. Aguado-Sierra, *et al.* Evidence of a dominant backward-

propagating "suction" wave responsible for diastolic coronary filling in humans attenuated in left ventricular hypertrophy. *Circulation* 113:1768–1778, 2006.

[8]Dunn, A. C., and T. D. Zaveri. Macroscopic friction coefficient measurements on living endothelial cells. *Tribol. Lett.* 27(2):233–238, 2007.

[9]Ene, F., P. Delassus, and L. Morris. The influence of computational assumptions on analysing abdominal aortic aneurysm haemodynamics. *Proc. Inst. Mech. Eng. H* 228(8):768–780, 2014.

[10]Ethier, C. R., and A. C. Simmons. Introduction to Biomechanics. From Cells to Organisms. New York: Cambridge University Press, 2007.

[11]Fedel, M., F. Tessarolo, P. Ferrari, C. Lösche, N. Ghassemieh, G. M. Guarrera, *et al.* Functional properties and performance of new and reprocessed coronary angioplasty balloon catheters. *J. Biomed. Mater. Res.* 78B(2):364–372, 2006.

[12]Gielen, H., O. Daniels, and H. van Lier. Natural history of congenital pulmonary valvar stenosis: an echo and Doppler cardiographic study. *Cardiol. Young* 1999(9):129–135, 1999.

[13]Johnston, K., P. Sharma, and J. Oshinski. Coronary artery flow measurement using navigator echo gated phase contrast magnetic resonance velocity mapping at 3.0T. *J. Biomech.* 41:508–602, 2008.

[14]Kamangar, S., G. Kalimuthu, I. A. Badruddin, A. Badarudin, N. J. Ahmed, and T. M. Khan. Numerical investigation of the effects of stenosis geometry on the coronary diagnostic parameters. *Sci. World J.* 2014:354946, 2014.

[15]Kinney, T. B., M. Fan, A. K. Chin, J. C. Finn, W. G. Hayden, and T. J. Fogarty. Shear force in angioplasty. *Am. J. Roentgenol.* 144(1):115–122, 1985.

[16]Kolandavel, M. K., E. T. Fruend, S. Ringgaard, and P. G. Walker. The effects of time varying curvature on species transport in coronary arteries. *Ann. Biomed. Eng.* 34(12):1820–1832, 2006.

[17]Kousera, C. A., S. Nijjer, R. Torii, R. Petraco, S. Sen, N. Foin, A. D. Hughes, D. P. P. Francis, X. J. Xu, and J. E. Davies. Patient-specific coronary stenoses can be modelled using a combination of OCT and flow velocities to accurately predict hyperemic pressure gradients. *IEEE Trans. Biomed. Eng.* 61:1902–1913, 2014.

[18]Lee, R. T., A. J. Grodzinsky, E. H. Frank, R. D. Kamm, and F. J. Schoen. Structure-dependent dynamic mechanical behavior of fibrous caps from human atherosclerotic plaques. *Circulation* 83:1764–1770, 1991.

[19]Leung, J. H., A. R. Wright, N. Cheshire, *et al.* Fluid structure interaction of patient specific abdominal aorta aneurysms: a comparison with solid stress models. *BioMed. Eng. OnLine* 5:33, 2006.

[20]Malve, M., A. Garcia, J. Ohayon, and M. A. Martinez. Unsteady blood flow and mass transfer of a human left coronary artery bifurcation FSI vs CFD. *Int. Commun. Heat Mass Transf.* 39:745–751, 2012.

[21]Mamada, K., H. Kosukegawa, V. Fridrici, P. Kapsa, and M. Ohta. Friction properties of PVA-H/steel ball contact under water lubrication conditions. *Tribol. Int.* 44(7):757–763, 2011.

[22]McDaniel, M. C., E. M. Galbraith, A. M. Jeroudi, O. R. Kashlan, P. Eshtehardi, *et al.* Localization of culprit lesions in coronary arteries of patients with ST-segment elevation myocardial infarctions: relation to bifurcations and curvatures. *Am. Heart J.* 161:508–515, 2011.

[23]Meng, S., H. Stefan, H. Geyer, F. da Luciano, M. P. Viana, and W. J. Weninger. Objective characterization of the course of the parasellar internal carotid artery using mathematical tools. *Surg. Radiol. Anat.* 30(6):519–526, 2008.

[24]Morris, L., P. Delassus, A. Callanan, M. Walsh, F. Wallis, P. Grace, and T. McGloughlin. 3-D numerical simulation of blood flow through models of the human aorta. *J. Biomech. Eng.* 127(5):767–775, 2005.

[25]Nichols, W. W., and M. F. Rourke. McDonald's Blood Flow in Arteries (5th ed.). Boca Raton: Taylor & Francis, 2005.

[26]O'Flynn, P., G. O'Sullivan, and A. Pandit. Methods for three-dimensional geometric characterization of the arterial vasculature. *Ann. Biomed. Eng.* 35(8):1368–1381, 2007.

[27]O'Flynn, P., G. O'Sullivan, and A. Pandit. Geometric variability of the abdominal aorta and its major peripheral branches. *Ann. Biomed. Eng.* 38(3):824–840, 2010.

[28]Pao, Y. C., J. T. Lu, and E. L. Ritman. Bending and twisting of an in vivo coronary artery at a bifurcation. *J. Biomech.* 25(3):287–295, 1992.

[29]Papaharilaou, Y., J. A. Ekaterinaris, E. Manousaki, *et al.* A decoupled fluid structure approach for estimating wall stress in abdominal aortic aneurysms. *J. Biomech.* 40:367–377, 2007.

[30]Perktold, K., and G. Rappitsch. Computer simulation of local blood flow and vessel mechanics in a compliant carotid artery bifurcation model. *J. Biomech.* 28:845–856, 1995.

[31]Pivkin, I. V., P. D. Richardson, D. H. Laidlaw, and G. E. Karniadakis. Combined effects of pulsatile flow and dynamic curvature on wall shear stress in a coronary artery bifurcation model. *J. Biomech.* 38:1283–1290, 2005.

[32]Prosi, E., K. Perktold, Z. Ding, and M. H. Friedman. Influence of curvature dynamics on pulsatile coronary artery flow in a realistic bifurcation model. *J. Biomech.* 37:1767–1775, 2004.

[33]Rennie, A. C., P. L. Dickrell, and W. G. Sawyer. Friction coefficient of soft contact lenses: measurement and modelling. *Tribol. Lett.* 18(4):499–504, 2005.

[34]Rieu, R., P. Barragan, V. Garitey, P. O. Roquebert, J. Fuseri, P. Commeau, *et al.* Assessment of the trackability, flexibility, and conformability of coronary stents: A comparative analysis. *Catheter Cardiovasc. Interv.* 59(4):496–503, 2003.

[35]Samady, H., P. Eshtehardi, M. C. McDaniel, J. Suo, S. S. Dhawan, C. Maynard, L. H. Timmins, A. A. Quyyumi, and D. P. Giddens. Coronary artery wall shear stress is associated with progression and transformation of atherosclerotic plaque and arterial remodeling in patients with coronary artery disease. *Circulation* 124:779–788, 2011.

[36]Schmidt, W., N. Grabow, P. Behrens, and K. P. Schmitz. Trackability, crossability, and pushability of coronary stent systems—an experimental approach. *Biomed. Tech. (Berl.)* 47(1):124–126, 2002.

[37]Scotti, C. M., and E. A. Finol. Compliant biomechanics of abdominal aortic aneurysms: a fluid-structure interaction study. *Comput. Struct.* 85:1097–1113, 2007.

[38]Scotti, C. M., A. D. Shkolnik, S. C. Muluk, *et al.* Fluid-structure interaction in abdominal aortic aneurysms: effects of asymmetry and wall thickness. *BioMed. Eng. OnLine* 4:64, 2005.

[39]Shaw, J. A., B. A. Kingwell, A. S. Walton, J. D. Cameron, P. Pillay, C. D. Gatzka, *et al.* Determinants of coronary artery compliance in subjects with and without angiographic coronary artery disease. *J. Am. Coll. Cardiol.* 39(10):1637–1643, 2002.

[40]Sinusas, A. J., X. Papademetris, R. T. Constable, D. P. Dione, M. D. Slade, P. Shi, and J. S. Duncan. Quantification of 3-D regional myocardial deformation: shape-based analysis of magnetic resonance images. *Am. J. Physiol. Heart Circ. Physiol*. 281:H698–H714, 2001.

[41]Steinman, D. A., Y. Hoi, P. Fahy, L. Morris, *et al*. Variability of CFD solutions for pressure and flow in a giant aneurysm: the SBC2012 CFD challenge. *J. Biomech. Eng*. 135(2):021016, 2013. doi:10.1115/1.4023382.

[42]Szabadits, P., Z. Puskas, and J. Dobranszky. Flexibility and trackability of laser cut coronary stent systems. *Acta Bioeng. Biomech*. 11(3):11–18, 2009.

[43]Takashima, K., R. Shimomura, T. Kitou, H. Terada, K. Yoshinaka, and K. Ikeuchi. Contact and friction between catheter and blood vessel. *Tribol. Int*. 40(2):319–328, 2007.

[44]Vavuranakis, M., I. Stamatopoulos, T. G. Papaioannou, S. Nikolopoulos, K. Toutouzas, and C. Stefanadis. Alterations of pressure waveforms along the coronary arteries and the effect of microcirculatory vasodilation. *Int. J. Cardiol*. 117:254–259, 2007.

[45]Weydahl, E. S., and J. E. Moore. Dynamic curvature strongly affects wall shear rates in a coronary artery bifurcation model. *J. Biomech*. 34:1189–1196, 2001.

[46]Whittaker, D. R., J. Dwyer, and M. F. Fillinger. Prediction of altered endograft path during endovascular abdominal aortic aneurysm repair with the gore excluder. *J. Vasc. Surg*. 41(4):575–583, 2005.

[47]Wijesinghe, L. D., D. J. A. Scott, and D. Kessel. Analysis of renal artery geometry may assist in the design of new stents for endovascular aortic aneurysm repair. *Br. J. Surg*. 84(6):797–799, 1997.

[48]Williams, M. J. A., R. A. H. Stewart, C. J. S. Low, and G. T. Wilkins. Assessment of the mechanical properties of coronary arteries using intravascular ultrasound: an in vivo study. *Int. J. Card. Imaging* 15(4):287–294, 1999.

[49]Wood, N. B., S. Z. Zhao, A. Zambanini, M. Jackson, W. Gedroyc, S. A. Thom, A. D. Hughes, and X. Y. Xu. Curvature and tortuosity of the superficial femoral artery: a possible risk factor for peripheral arterial disease. *J. Appl. Physiol*. 101(5):1412–1418, 2006.

[50]Yin, C. P. F., Y. R. K. Strumpf, P. H. Chew, and S. L. Zeger. Quantification of the mechanical properties of noncontracting canine myocardium under simultaneous biaxial loading. *J. Biomech*. 20(6):577–589, 1987.

[51]Zeng, D., Z. Ding, M. H. Friedman, and C. R. Ethier. Effects of cardiac motion on right coronary artery hemodynamics. *Ann. Biomed. Eng*. 31:420–429, 2003.

[52]Zhao, S. Z., X. Y. Xu, A. D. Hughes, *et al*. Blood flow and vessel mechanics in a physiologically realistic model of a human carotid arterial bifurcation. *J. Biomech*. 33:975–984, 2000.

[53]Zheng, S., and Y. Qi. Motion estimation of 3D coronary vessel skeletons from X-ray angiographic sequences. *Comput. Med. Imaging Graph*. 35(5):353–364, 2011.

[54]Zoarski, G. H., J. M. Mathis, and J. R. Hebel. Performance characteristics of microcatheter systems in a standardized tortuous pathway. *Am. J. Neuroradiol*. 19(8):1571–1576, 1998.